Check for updates

Zuo Chao (Orcid ID: 0000-0002-1461-0032)

ma ying (Orcid ID: 0000-0002-3105-375X)

Accepted Article

phys. stat. sol. (a) 201, No. 13 (2004) / www.pss-rapid.com R

RESEARCH ARTICLE

Reflectional quantitative differential phase microscopy using polarized wavefront phase modulation

Ying Ma[1,†] | Taiqiang Dai[2,†] | Lan Yu[1] | Lin Ma[1] | Sha An[1] | Yang Wang[1] | Min Liu[1] | Juanjuan Zheng[1] | Liang Kong*[,2] | Chao Zuo[1] | Peng Gao*[,1]

[1] School of Physics, Xidian University, Xi'an, China

[2] State Key Laboratory of Military Stomatology & National Clinical Research Center for Oral Diseases & Shaanxi Clinical Research Center for Oral Diseases, Department of Oral and Maxillofacial Surgery, School of Stomatology, The Fourth Military Medical University, Xi'an, China

†Equal contributor

*** Correspondence**
Liang Kong
School of Stomatology, The Fourth Military Medical University, Xi'an 710032, China
Peng Gao
School of Physics, Xidian University, Xi'an 710071, China
Email: liangkong2014@163.com (L. K.) and peng.gao@xidian.edu.cn (P. G.)

Quantitative phase microscopy (QPM), as a label-free and nondestructive technique, has been playing an indispensable tool in biomedical imaging and industrial inspection. Herein, we introduce a reflectional quantitative differential phase microscopy (termed RQDPM) based on polarized wavefront phase modulation and partially coherent full-aperture illumination, which has high spatial resolution and spatio-temporal phase sensitivity and is applicable to opaque surfaces and turbid biological specimens. RQDPM does not require additional polarized devices and can be easily switched from reflectional mode to transmission mode. In addition, RQDPM inherits the characteristic of high axial resolution of differential interference contrast microscope (DIC), thereby providing topography for opaque surfaces. We experimentally demonstrate the reflectional phase imaging ability of RQDPM with several samples: semiconductor wafer, thick biological tissues, red blood cells (RBCs), and Hela cells. Furthermore, we dynamically monitor the flow state of microspheres in a self-built microfluidic channel by using RQDPM converted into the transmission mode.

KEYWORDS
reflectional imaging, quantitative differential phase, polarized wavefront modulation, label free, partially coherent, full-aperture illumination

1 | INTRODUCTION

This article has been accepted for publication and undergone full peer review but has not been through the copyediting, typesetting, pagination and proofreading process which may lead to differences between this version and the Version of Record. Please cite this article as doi: 10.1002/jbio.202200325

This article is protected by copyright. All rights reserved.

18640648, ja, Downloaded from https://onlinelibrary.wiley.com/doi/10.1002/jbio.202200325 by Nanjing University Of Science, Wiley Online Library on [12/02/2023]. See the Terms and Conditions (https://onlinelibrary.wiley.com/terms-and-conditions) on Wiley Online Library for rules of use; OA articles are governed by the applicable Creative Commons License

The development of microscopy invites breakthroughs in life science and industrial inspection. Optical microscopy, especially fluorescence microscopy, develops rapidly, providing a versatile tool for visualizing structures of interest [1-6]. Meanwhile, reflectional imaging techniques are needed to acquire 3D profiles of strong scattering biological samples or opaque industrial devices.

Optical coherence tomography (OCT) based on low coherence interference is a mature label-free microscopic technology for imaging deep tissues without phototoxicity and photobleaching, and it is now gradually becoming one of the important medical diagnosis devices [7, 8]. With the phase information preserved in OCT recovered by solving the inverse scattering problems, one can visualize the transparent structures with high contrast [9]. Quantitative phase microscopy (QPM) recovers the structure of a sample by exploiting the phase information of object wave from the sample. QPM works in a noninvasive and label-free manner, and it has tremendous applications in life science research and quality inspection of micro-nano devices [10, 11]. Among different QPM approaches, digital holographic microscopy (DHM), combining optical interference and digital processing, can get access to the sample's amplitude and phase information [12-18]. The poor stability in traditional off-axis DHM is overcome by using a common-path point diffraction configuration [15]. The fringe contrast and phase recovery accuracy of point-diffraction DHM are improved by using a polarized grating and the partially coherent illumination [14, 18]. While, such point-diffraction DHM still suffers from its limite spatial resolution. The spatial resolution, as well as the tomographic imaging capability, of DHM can be dramatically improved by using oblique illumination and frequency spectrum projection based reconstruction [16, 17]. However, the price for this is the reduction of temporal resolution. Furthermore, confocal DHM based on a Mirau objective lens can detect the turbid translucent tissue without additional staining [19]. Overall, DHM has been widely applied in quantitative imaging of thick tissues or opaque samples, while it still faces tradeoffs among spatial resolution, temporal resolution, and phase sensitivity. It is meant that conventional DHM can only guarantee a high spatial resolution or high temporal resolution, not the two at the same time.

In recent years several compact and low-cost QPM approaches based on light emitting diodes (LEDs) have been proposed, which can provide phase maps with high image quality for different types of samples. Among these approaches, Fourier ptychographic microscopy (FPM) performs phase imaging with a high spatial resolution and a large field of view (FOV) at the same time [20-23], by utilizing multidirectional illuminations and an iterative computational technique. Recently, reflective FPM has been implemented for opaque samples by using a parabolic mirror and a dark illuminator [24, 25]. Generally, FPM is low-cost and easy to implement, while it requires dozens of raw data and thereby has a limited temporal resolution. Furthermore, quantitative differential phase contrast (qDIC) microscopy using asymmetrical partially coherent illumination from an LED array was proposed, which was implemented in both transmission and reflective modes for different types of applications [26-28]. This method qDIC is also low-cost, while in qDIC the maximum illumination angle should be close to the maximum NA-limited angle of the detection objective lens. Otherwise, the low-frequency sample information will be lost. Moreover, QPM based on recording diffraction intensities at different axial positions, for example, transport of intensity equation (TIE) based QPM, has been playing an important role in the quantitative phase imaging domain owing to its unique characteristics of ease of implementation [29, 30]. Recently, a specially constructed prism was utilized to simultaneously acquire multiple diffraction intensities of a sample at different axial planes, from which the high-resolution 3D phase distribution of the sample is then calculated [31].

The invention of spatial light interference microscopy (SLIM) is a critical leap in the development of phase contrast microscopy, or specifically, an evolution from qualitative display to quantitative analysis [32-35]. Owing to the common path structure and wide-spectrum illumination, SLIM has been extensively used in cell growth, cell migration, and drug screening, etc. Later, by using an annular LED illuminator, our group proposed flat-fielding quantitative phase contrast microscopy (FF-QPCM) for long-term continuous observation of organelles inside live cells including their dynamics, such as mitochondria and endoplasmic reticulum [36]. FF-QPCM has a remarkable spatiotemporal resolution of 245 nm and 250 FPS. In addition, reflective quantitative phase contrast microscopy (RQPCM) was then implemented for phase imaging of opaque surfaces [37]. Since the unscattered frequency components of a sample need to be phase modulated in FF-QPCM and RQPCM, strong scattering samples with very few unscattered components are not applicable in these methods. To impart excellent optical sectioning capability to QPM, Popescu et al. proposed gradient light interference microscopy (GLIM) that incorporates phase-shifting operation into a commercial Nomarski differential interference contrast microscope (DIC), rendering the 3D tomography of embryos [38]. Subsequently, reflective GLIM was implemented for opaque samples [39]. It is remarkable that the usage of the Wollaston prism limits the potential of GLIM to some extent. On the other hand, phase imaging based on quadri-wave lateral shearing interferometry requires only one measurement to recover the phase information of a sample by means of an orthogonal carrier-frequency

Accepted Article

18640648, ja, Downloaded from https://onlinelibrary.wiley.com/doi/10.1002/jbio.202200325 by Nanjing University Of Science, Wiley Online Library on [12/02/2023]. See the Terms and Conditions (https://onlinelibrary.wiley.com/terms-and-conditions) on Wiley Online Library for rules of use; OA articles are governed by the applicable Creative Commons License

multiplexing strategy [40]. The spatial resolution of this method is still limited due to the plane-wave illumination.

In this work, we introduce a new reflectional quantitative differential phase microscopy (RQDPM) based on polarized wavefront phase modulation. RQDPM utilizes the polarization-dependent characteristic of a phase-type SLM to divide the object wave into two identical copies with a certain shear distance. When loading different modulation images to the SLM, DIC images with different shearing directions and phase shifts can be obtained. Owing to the partially coherent full-aperture illumination and common path interference structure, RQDPM possesses high spatio-temporal resolution and phase sensitivity. We demonstrate the quantitative phase imaging capability of RQDPM by imaging a semiconductor wafer, thick biological tissues, human RBCs, and Hela cells. Furthermore, we demonstrate that RQDPM converted into transmission mode can be used as a real-time and high-sensitivity tool for monitoring the flow speed of microspheres in a microfluidic channel. We imagine that our system will contribute to life science and industrial inspection.

2 | METHODS

RQDPM system and phase recovery principle

The schematic diagram of RQDPM is shown in Figure 1, where a narrow-band LED (470 ± 20 nm, central spectrum ± half width) is used as the illumination source. A diffuser (Diff) is placed close to the LED, and it is exactly at the focal plane of lens L4. The emitted light from LED is scattered by the diffuser and is collimated into different phase waves in different directions. The diffuser is imaged onto the pupil plane of the objective lens by a telescope system L4-L1, and hereby an extended light source with full-aperture illumination is formed. Then the sample is illuminated at different angles spanning the numerical aperture range of the objective lens, and therefore the spatial resolution is maximized. Notably, a beam splitter (BS) is placed on the imaging plane instead of the Fourier plane to make the system more compact. The adverse effect of the scratches or dirty spots brought by the beam splitter can be suppressed by subtracting the background phase image that is obtained in the absence of a sample. For opaque samples, the illumination beam illuminates the sample from the bottom, and the wave reflected by the sample is then collected by the same objective lens. For some transparent samples, to verify the system's performance, a mirror M1 is placed on top of the sample, so that the reflected object wave contains the transmittance information of the sample. For both cases, the collected object waves are then magnified and relayed by two telescope systems Obj-L1 and L2-L3 to a sCMOS plane (Zyla 4.2, Andor, UK). In the middle Fourier plane of L2-L3, a reflective phase-type spatial light modulator (MSP1920-400-800-HSP8, Meadowlark Optics, USA) is positioned to modulate the spectrum of the object wave. To form a shearing interferometer, two linear polarizers P1 and P2 are installed before and after the spatial light modulator (SLM) with their polarization direction ~ 45° with respect to the action axis of the SLM (*x*-axis). Notably, the phase-type SLM has the unique characteristics of polarization-dependent modulation. Specifically, it only modulates the *x*-polarized light, while it only acts as a plane mirror for the *y*-polarized light. As a result, when a linear phase map is loaded to the SLM, two copies of object waves will be generated with a shear distance in-between, as shown in Figure 1. And the shear vector can be expediently adjusted by changing the slope and inclination direction of the linear phase map. Without loss of generality, the phase map loaded to the SLM can be normally expressed as:

$$\varphi_{carrier,i}(\vec{r},\delta\varphi_i) = Wr\left\{\frac{2\pi\,\vec{r}\cdot\vec{r}_0}{\lambda f_3}+\delta\varphi_i\right\}, \tag{1}$$

where $\vec{r}=(x, y)$ is the transverse spatial vector on the SLM plane, $\vec{r}_0=(x_0, y_0)$ the shear vector on the sCMOS plane, λ the central wavelength of the LED, f_3 the focal length of the lens L3, and $\delta\varphi_i = 0, 0.5\pi, \pi$, and 1.5π is the phase shift in the *ith* phase shifting operation. $Wr\{\cdot\}$ denotes the wrapping operation that folds the phase in $[0, 2\pi]$. When the SLM loads the pattern expressed in Equation 1, the final object waves arriving at the sCMOS plane are the summation of two copies of object waves without and with a lateral shear $\vec{r}_0$, and therefore the corresponding intensity distribution on the sCMOS plane can be written as:

$$\begin{aligned} I_i\left(\vec{R},\vec{r}_0,\delta\varphi_i\right) &= s^2(\vec{R})+s^2(\vec{R}-\vec{r}_0) \\ &+2\,|\,s(\vec{R})\,|\cdot|\,s(\vec{R}-\vec{r}_0)\,|\cdot\cos\left(\Delta\varphi(\vec{R})+\delta\varphi_i\right), \end{aligned} \tag{2}$$

with $\vec{R}=(x', y')$ being the transverse spatial vector on the sCMOS plane, $s(\vec{R})$ and $s(\vec{R}-\vec{r}_0)$ the object waves without and with a shear. And $\Delta\varphi(\vec{R})=\varphi(\vec{R}-\vec{r}_0)-\varphi(\vec{R})$ is the phase difference between the two overlapped object waves $s(\vec{R}-\vec{r}_0)$ and $s(\vec{R})$. One can simply adjust the lateral shear $\vec{r}_0$ by changing the slope and inclination direction of the phase pattern on the SLM. The phase difference $\Delta\varphi(\vec{R})$ can be well solved from the recorded I_1, I_2, I_3, and I_4 by using the phase shifting algorithm. Then, the phase derivative of the sample $\nabla_r\varphi(\vec{R})$ along the *r*-direction can be approximated as the quotient of the phase difference $\Delta\varphi(\vec{R})$ and the related shear shift when the shear is about half of the lateral resolution of the system [38,39,41].

Accepted Article

18640648, ja, Downloaded from https://onlinelibrary.wiley.com/doi/10.1002/jbio.202200325 by Nanjing University Of Science, Wiley Online Library on [12/02/2023]. See the Terms and Conditions (https://onlinelibrary.wiley.com/terms-and-conditions) on Wiley Online Library for rules of use; OA articles are governed by the applicable Creative Commons License

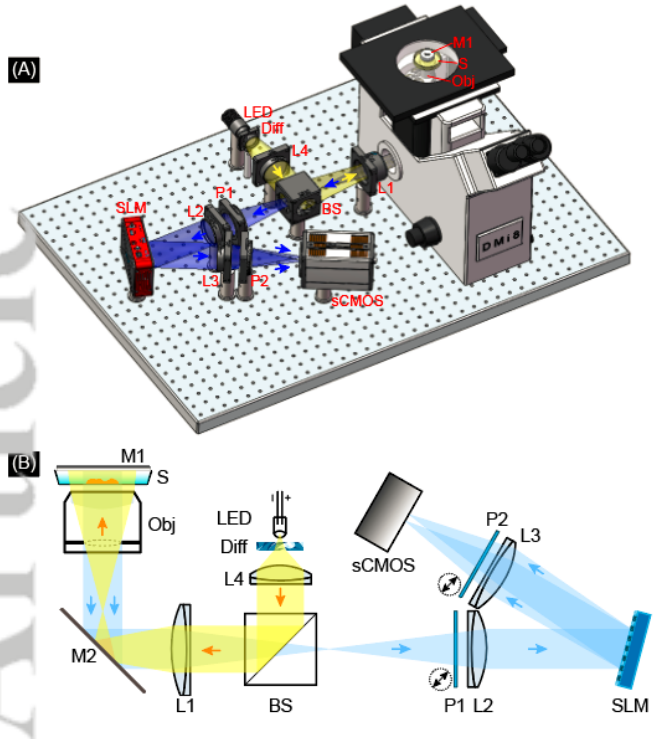

FIGURE 1 Schematic diagram of RQDPM. 3D drawing (A) and 2D line sketch (B) of the system. Yellow light represents the illumination beam while blue one the reflected object waves. BS, beam splitter; Diff, diffuser; L, lens; M, mirror; Obj, objective lens; P, polarizer; S, sample; SLM, spatial light modulator; sCMOS, scientific complementary metal oxide semiconductor.

In practice, we obtain the phase derivatives $\nabla_x\varphi(\vec{R})$ and $\nabla_y\varphi(\vec{R})$ along the x-axis and y-axis by choosing $\vec{r}_0$ along the x and y directions in sequence. Then, the quantitative phase distribution of the object wave is obtained by integrating the two phase derivatives with the Frankot-Chellappa algorithm [42]:

$$\varphi(\vec{R}) = \Im^{-1}\left\{\frac{-jk_x\cdot\Im\left[\nabla_x\varphi(\vec{R})\right]-jk_y\cdot\Im\left[\nabla_y\varphi(\vec{R})\right]}{2\pi\left(k_x^2+k_y^2\right)+\alpha}\right\}. \quad (3)$$

Here, $\Im\{\cdot\}$ and $\Im^{-1}\{\cdot\}$ represent the forward and inverse Fourier transforms, and $\vec{k}=(k_x, k_y)$ is the transverse frequency vector on the sCMOS plane. α is a regulation parameter to prevent the denominator from approaching zero near the low-frequency region, which is conducive to background homogenization. Equation 3 implies that RQDPM can recover the phase distributions of samples quantitatively in the reflectional mode. Furthermore, the combination of phase shifting operation and partially coherent illumination from the diffused LED can suppress the multiple scattering from turbid structures [39], yielding a high-quality phase image. Notably, gradient light interference microscopy (GLIM) [38] uses a Wallaston prism to generate two copies of object waves with a lateral shear, and then uses a SLM to perform phase shifting by introducing phase delay to one of the object waves. In GLIM, phase derivative along a single direction was generated, from which the phase is reconstructed. By contrast, our RQDPM uses a SLM to generate DIC interferograms along two orthogonal directions by loading different phase masks in sequence, enhancing phase reconstruction accuracy, simplifying the system, and making the system easier to couple with other imaging modes.

In addition, our RQDPM can easily switch between the reflection and transmission modes, which share the same detection path. The transmission mode requires an extra annular illuminator containing several LEDs, and the details can be found in our previous work [41]. In contrast to the transmission mode, RQDPM operates at the full-aperture illumination, and uses the same objective lens for illumination and detection simultaneously. This not only maximizes the frequency coverage range but also opens the door to integration with other imaging technologies. It should be noted that a mirror is placed on top of the sample to provide a reasonable reflectional wave when RQDPM is used for imaging transparent samples in the reflection mode. In this case, the light beam passes the sample twice compared with the transmission quantitative differential phase microscopy (TQDPM) [41]. On one side, this can enhance the sensitivity to the phase retarder of the sample. On the other side, this could possibly cause additional disturbing diffraction patterns from the sample or image disturbances in case the incident light is not passing the sample exactly perpendicular to the sample plane. Though the phase recovery principle of RQDPM and TQDPM is the same, RQDPM benefits full-aperture illumination for any type of objective lens to maximize the spatial resolution, which is impossible in TQDPM unless it uses a water-immersion condenser objective lens with a high numerical aperture. Therefore, when the spatial resolution permits, it is recommended to use TQDPM [41] to image transparent samples. It is also worth comparing RQDPM with reflective quantitative phase contrast microscopy (RQPCM) [37]. In RQPCM, only the unscattered components are phase modulated, which prevents its application from strong scattering samples with very few unscattered components. While, RQDPM is based on DIC concept implemented by using polarized wavefront phase modulation on the pupil plane. RQDPM does not require precise modulation to specific frequency components, and therefore, it is more suitable for samples with different degrees of scattering compared to RQPCM.

2.2 | System calibration

The accurate phase modulation of the SLM is crucial for phase imaging and phase recovery of RQDPM. We determine the phase response curve of the SLM versus the loaded gray

Accepted Article

18640648, ja, Downloaded from https://onlinelibrary.wiley.com/doi/10.1002/jbio.202200325 by Nanjing University Of Science, Wiley Online Library on [12/02/2023]. See the Terms and Conditions (https://onlinelibrary.wiley.com/terms-and-conditions) on Wiley Online Library for rules of use; OA articles are governed by the applicable Creative Commons License

level through a self-interference method [43]. To be specific, a mirror is used as the sample to reflect the illumination light to the SLM. Meanwhile, an additional lens is provisionally mounted between the sCMOS and lens L3 for imaging the SLM plane to the sCMOS camera. The gray level of the SLM pixels increases from 0 to 255 step by step, and the modulated light by the SLM interferes with the light plainly reflected (unmodulated light) by the SLM. The camera records the interference patterns one by one. Then, the look-up table (LUT) between the intensity of the interference pattern and the loaded gray level is obtained and shown as the black curve in Figure 2B. The relation between the generated phase and the loaded gray value can be calculated from the intensity curve, and the result is shown with the red curve in Figure 2B. Eventually, any desired phase value can be generated on any pixel of the SLM. For instance, the images in Figure 2A show four phase patterns $\varphi_{carrier,i}(\vec{r}, \delta\varphi_i)$ with $\delta\varphi_i$ switched four times (0, 0.5π, π, and 1.5π) when the shear is along the *x*-axis. It should be noted that all phase values loaded to the SLM should be wrapped between 0 and 2π to accommodate the effective range of the SLM, as shown in Figure 2A.

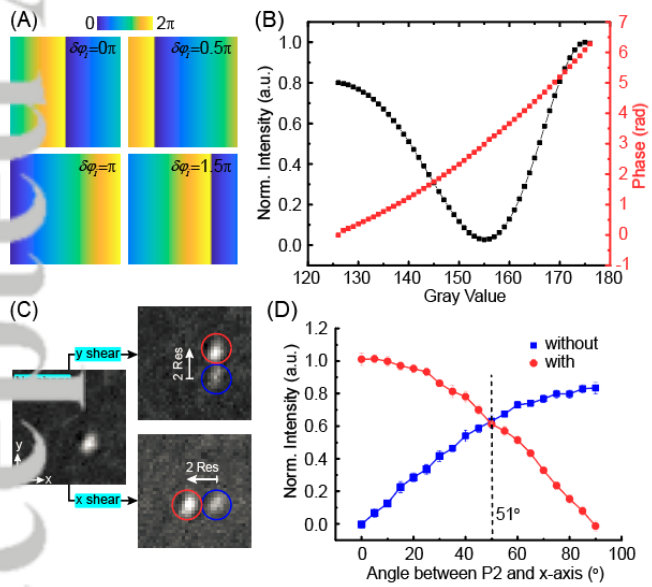

FIGURE 2 Calibration of RQDPM. (A) Four wrapped phase patterns $\varphi_{carrier,i}(\vec{r}, \delta\varphi_i)$ loaded to the SLM for generating the shear along the *x*-axis. (B) Normalized intensity (black) and phase value (red) of a SLM pixel in response to different gray level loaded to the SLM. (C) Images of a particle without and with the shear along *x*- and *y*-axes. A shear of twice the lateral resolution of the system was set. (D) Normalized mean intensity values of the two shear images of the same particle formed by the modulated light (red) and unmodulated light (blue) with respect to the angle between polarizer P2 and the *x*-axis.

On the other hand, reflective SLMs have different reflection efficiency for the linear polarized light in different directions. Specifically, the SLM modulates only the *x*-polarized light and has no effect on the *y*-polarized light. Therefore, when the polarizer P2 is installed with its polarization azimuth 45° with respect to the *x*-axis, two shear images for a single particle are formed. One is from the modulated light, while the other one is from the unmodulated light, as is shown in Figure 2C. To quantitatively analyze the polarization-dependent phase modulation effect of the SLM, we rotated polarizer P2 step by step and measured synchronously the mean intensity of the two shear images of the same particle in Figure 2C, and the result is shown in Figure 2D. Clearly, the two intensity curves change with the angle in the opposite way. When the angle between polarizer P2 and the *x*-axis is about 51°, the two images have almost the same intensity. Therefore, to ensure the accuracy of the phase recovery, we keep the angle of the polarizer P2 as 51° in the subsequent experiments.

2.3 | Sample preparation

RQDPM has been applied to imaging a variety of samples, including polystyrene microbeads, fixed Hela cells, and mouse submandibular gland tissue slices, etc. For the polystyrene microbeads sample, 1 μL of 1-μm polystyrene microbeads stock solution containing 5% solid content was diluted into 2000 μL of deionized water and shaken evenly by a vortex mixer at 1000 revolutions per minute for 2 minutes. The homogenized solution was then transferred to a glass-bottom petri dish (FD5040-100, World Precision Instrument, USA) and incubated for 30 min at room temperature. Due to the gravity and the poly-D-lysine coating the microbeads on the glass surface were immobilized stably.

The Hela cells in Figure 9 (CL-0101, Procell Life Science & Technology, China) were cultured in DMEM medium (TM 41090036, Gibco) containing 10% FBS (SF0007001, HyClone) and 1% penicillin–streptomycin (J200049, HyClone). Then, the cells were moved to a glass-bottom petri dish (FD5040-100, World Precision Instrument, USA) at 37 °C with 5% CO_2 for 24 hours before being fixed with 4% formaldehyde. 5-μm polystyrene microbeads (DRM05, Huge Biotechnology, China) were poured on the inner edge of the petri dish to support the mirror M1 when the fixed Hela cells were imaged with RQDPM. The cell-coated glass bottom of the petri dish fits the working distance of the air objective lens (20×/0.3, Leica, Germany).

The mouse submandibular gland tissue slices in Figure 6 were prepared from a 6-week-old rat. The obtained glands from a rat after euthanasia were frozen in an optimal cutting temperature compound (SAKURA, Japan) at -20 ℃ for 30 minutes. The frozen submandibular glands were then cut into 7-μm slices by Cryastat (CM1850, Leica) and placed onto the glass bottom of a petri dish. The tissue slices were then fixed with cold acetone for 15 minutes and rinsed in phosphate buffer saline (PBS) before being imaged with RQDPM.

Accepted Article

18640648, ja, Downloaded from https://onlinelibrary.wiley.com/doi/10.1002/jbio.202200325 by Nanjing University Of Science, Wiley Online Library on [12/02/2023]. See the Terms and Conditions (https://onlinelibrary.wiley.com/terms-and-conditions) on Wiley Online Library for rules of use; OA articles are governed by the applicable Creative Commons License

The human blood samples were collected according to the routine collection procedure, and 10 μL of the original blood was dropped onto the surface of a 70 mm × 25 mm slide. After that, a 20 mm × 20 mm coverslip was put onto the blood and left for 30 min at room temperature. Then a human blood smear containing the red blood cells (RBCs) in Figure 7 was obtained. The thickness of the slide and the coverslip are both 0.17 mm. When the prepared blood sample is imaged with RQDPM, the side of the slide faces the objective lens, while the mirror M1 is placed onto the coverslip. In this case, RBCs in the blood sample are within the working distance of the air objective lens (20×/0.3, Leica, Germany).

3 | RESULTS

3.1 | Quantitative phase imaging of polystyrene microbeads

To validate the quantitative phase imaging capability of RQDPM, we measured 1-μm diameter polystyrene microbeads (DRM01, Huge Biotechnology, China). The microbeads are prepared according to the procedure in Part 2.3 and covered by a mirror M1 when imaged with RQDPM. Therefore, the scattered waves from these microbeads are reflected and collected from the bottom, as shown in Figure 1. It should be noted that the measured phase value in RQDPM is twice the expected value, and it is expressed as $\varphi(\vec{R})=4\pi\cdot h(\vec{R})\cdot\left(n(\vec{R})-n_0\right)/\lambda$, with n_0 being the refractive index (RI) of the surrounding medium, $n(\vec{R})$ and $h(\vec{R})$ the RI and height distributions of the sample. In the following experiments, we divide the phase value calculated in RQDPM by 2 to be consistent with its expected value. Figure 3A and Figure 3B are the calculated phase derivatives of a microbead along the *x*- and *y*-directions by RQDPM. And Figure 3C shows the recovered phase distribution of the microbead. A line crossing the bead through its center is extracted, and the phase distribution along the line is shown in Figure 3D. And the theoretical phase profile crossing the microbead center is shown as the red curve, from which we can clearly find that RQDPM can accurately recover the phase distribution of a microbead. The results imply that RQDPM can quantitatively recover the phase map of a sample with high signal-to-noise (SNR) ratio, which attributes to the partially coherent illumination and common path interference structure of RQDPM.

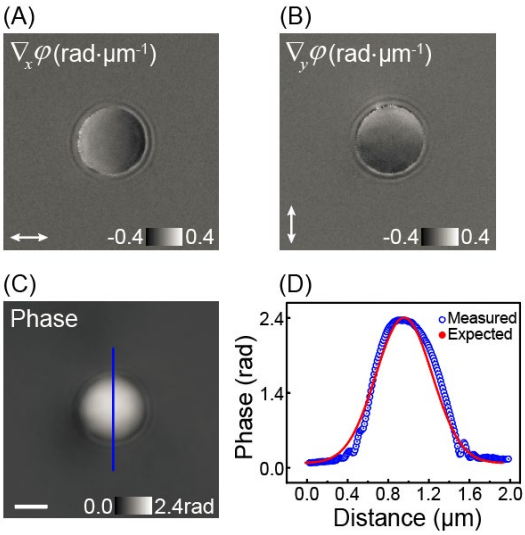

FIGURE 3 RQDPM imaging of a 1-μm polystyrene microbead. (A) Phase derivative along the *x*-axis. (B) Phase derivative along the *y*-axis. (C) Recovered phase map of the microbead. (D) Phase curve along the blue line in (C) with the red curve being the theoretically expected plot. The scale bar in (C) represents 0.5 μm.

3.2 | Quantitative morphology detection of opaque semiconductor wafer by RQDPM

With RQDPM, we performed non-contact imaging of an opaque semiconductor wafer, whose surface has many nanostructures generated via lithography. In this experiment, RQDPM was equipped with a 20×/0.3 objective lens. The actual semiconductor wafer exhibits colorful reflections on its surface due to the chromatic diffraction of nanostructures on white light, as shown in Figure 4A. There are many step-alike architectures on the wafer's surface. Using RQDPM, we reconstructed the 3D morphology of the step architectures, as shown in Figure 4B. The statistical data indicates that the height of the step structures is 1.2 ± 0.1 μm (mean ± s. d.). Interestingly, we find that there are many dot structures periodically distributed on the wafer surface, as shown in Figure 4C. Figure 4D shows the magnified image of two dot structures that are marked with a white box in Figure 4C, and the height profile along the blue line is shown in Figure 4E. When we analyzed dozens of dot structures by taking the cut lines crossing their centers and fitting the lines with Gaussian functions, the statistic tells that their diameter and height are 1.5 ± 0.1 μm and 100 ± 10 nm, respectively. In our previous work, we combined nano-imprinting strategy and transmission quantitative differential phase microscopy (TQDPM) to realize the high-sensitivity 3D inspection of silicon semiconductor wafers [41]. And as is mentioned before that RQDPM can be easily switched from reflectional mode to transmission mode, we use RQDPM and TQDPM to detect the same wafer for comparison. The comparison tells us that RQDPM can provide the topography for an opaque semiconductor wafer with a nanoscale axial sensitivity comparable to that of TQDPM.

Accepted Article

18640648, ja, Downloaded from https://onlinelibrary.wiley.com/doi/10.1002/jbio.202200325 by Nanjing University Of Science, Wiley Online Library on [12/02/2023]. See the Terms and Conditions (https://onlinelibrary.wiley.com/terms-and-conditions) on Wiley Online Library for rules of use; OA articles are governed by the applicable Creative Commons License

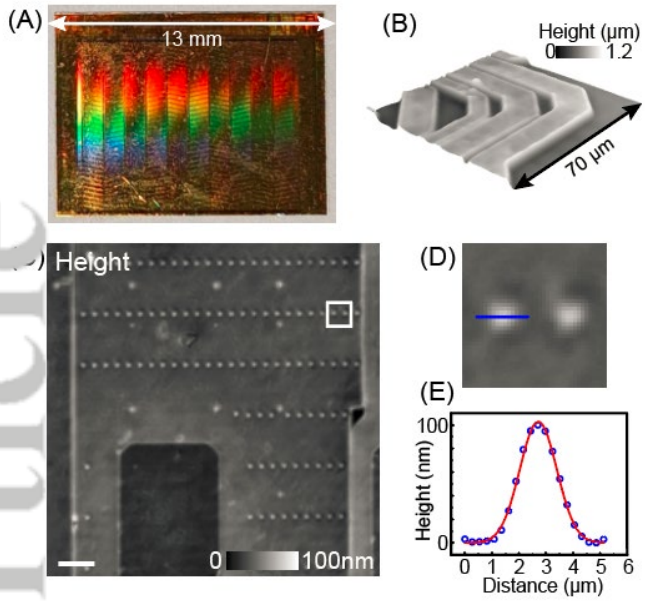

FIGURE 4 Quantitative phase imaging of a semiconductor wafer by RQDPM. (A) Real image of the semiconductor wafer. (B) A representative 3D morphology of step structures in (A). (C) Two-dimensional height distribution of dot structures. (D) Enlarged view of two dot structures that are marked with a white box in (C). (E) Height distribution (blue) along the blue line in (D) and its Gaussian fitting (red). The scale bar in (C) represents 14 μm.

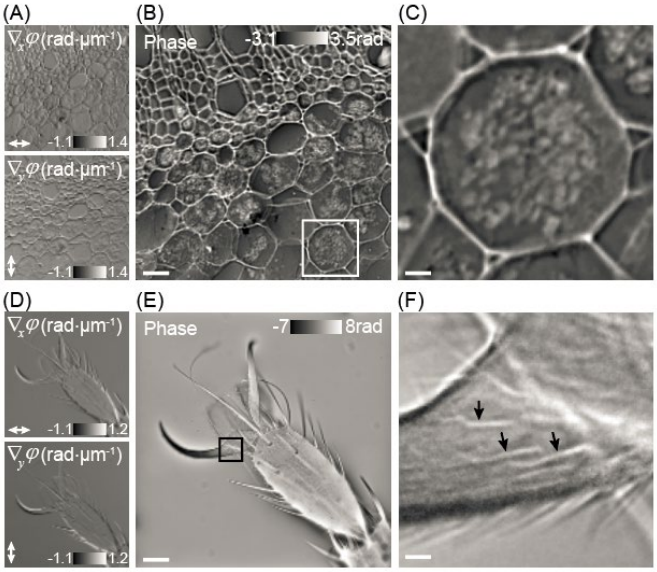

FIGURE 5 RQDPM imaging of thick biological tissue slices by using an air objective lens. Phase derivatives of the cross sections of a balloon flower stem (A) and a fly leg (D) along the x- and y-axes. Reconstructed phase maps of the balloon flower stem cross-section (B) and the fly leg cross-section (E). (C) and (F) are enlarged views of the areas marked with a white box in (B) and a black box in (E). The scale bars in (B), (C), (E), and (F) represent 24 μm, 5 μm, 55 μm, and 5 μm, respectively.

3.3 | Quantitative phase imaging of thick biological specimens by RQDPM

RQDPM was further verified for quantitative phase imaging of thick biological tissue slices by using different types of objective lenses. First, a slice of a balloon flower stem and a fly leg are successively imaged with RQDPM equipped with a 4× objective lens. Figures 5A-C are the results of a balloon flower stem cross-section. The upper and lower panels in Figure 5A are the calculated phase derivatives along the *x*- and *y*-axes. Figure 5B is the reconstructed phase image, of which a tubular structure marked with a white box is enlarged in Figure 5C. Notably, sieve tubular structures can be visualized with high contrast by RQDPM, as demonstrated in Figure 5C. Then a cross-section of a fly leg was imaged with RQDPM. The two images in Figure 5D are the phase derivatives along the *x*- and *y*-axes, and Figure 5E the reconstructed phase image. Interestingly, fluffs that function as precision sensor on the leg are clearly visible, and of note, Figure 5F shows some smaller ones with a mean diameter of ~ 1 μm. These two typical examples confirm that RQDPM with an air objective lens acts as a versatile tool for the observation of biological samples in reflectional mode, with which high-quality phase images of thick biological samples can be obtained.

Moreover, RQDPM equipped with an oil immersion objective lens (100×/1.44) was used for imaging a mouse submandibular gland tissue slice. Such tissue slice has a thickness of ~ 7 μm, and it was prepared according to the protocol in Part 2.3. Figure 6A shows the phase derivatives of the tissue slice along the *x*- and *y*-axes, and Figure 6B is the reconstructed phase image. The fine filamentous structures inside the tissue are clearly displayed, profiting from the full-aperture illumination in RQDPM. And a small FOV marked with a white box in Figure 6B is magnified and shown in Figure 6C. The quantitative analysis is then performed by plotting the phase distributions along the lines perpendicularly crossing the microfilaments and fitting them with a Gaussian function, as shown in Figure 6D. After analyzing the microfilaments at dozens of different locations, the average diameter of the microfilaments is measured as 300 ± 10 nm. The above proof-of-concept experiments indicate that RQDPM copes well with different samples.

Accepted Article

18640648, ja, Downloaded from https://onlinelibrary.wiley.com/doi/10.1002/jbio.202200325 by Nanjing University Of Science, Wiley Online Library on [12/02/2023]. See the Terms and Conditions (https://onlinelibrary.wiley.com/terms-and-conditions) on Wiley Online Library for rules of use; OA articles are governed by the applicable Creative Commons License

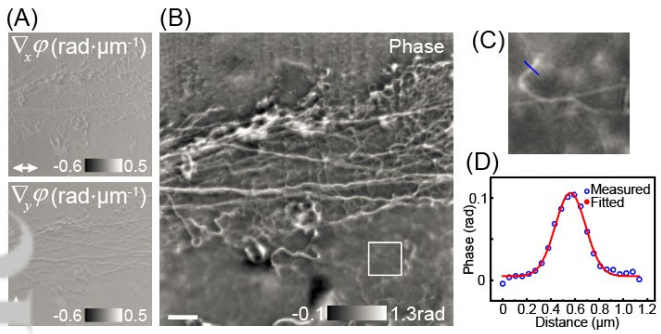

FIGURE 6 RQDPM imaging of a mouse submandibular gland tissue slice by using an oil immersion objective lens. (A) Phase derivatives along the x- and y-axes. (B) Recovered phase image. (C) Enlarged view of the area indicated with a white box in (B). (D) Phase distribution (blue dots) along the blue line in (C) and its Gaussian fitting (red curve). The scale bar in (B) represents 10 μm.

3.4 | Quantitative estimation of parameters of RBCs and Hela cells by RQDPM

To further demonstrate the reflectional imaging capability of the system under the partially coherent full full-aperture illumination, RQDPM was applied to quantitative detection of physical parameters of biological samples, including human red blood cells (RBCs) and Hela cells. As is generally known, accurate quantification of the morphology size and hemoglobin (Hb) content of RBCs is essential for diagnosing and monitoring many diseases, like anemias [44]. In particular, the dry Hb mass of RBCs has important clinical value, which is routinely obtained by clinical hematology analyzers based on the scattering of spherical RBCs [45]. Due to the characteristic doughnut shape, RBCs must undergo a spheroidization process, which complicates the testing process and leaves the RBCs in an abnormal morphological state [46]. In comparison, QPM can directly convert the retrieved phase into the dry Hb mass density of an investigated RBC in its natural state based on the linear relationship between the Hb refractive index (n) and Hb mass concentration (C), that is $n=\beta\times C+n_m$, with β being the refractive index increment and n_m the refractive index of the surrounding medium [47]. For this purpose, we use RQDPM equipped with a 20×/0.3 objective lens to image RBCs for quantifying their physical parameter. Considering the back-scattering wave from thin RBCs is weak, and the physical significance of the phase of the back-scattering wave is ambiguous, the human blood smear is covered by a mirror M1 on the top to provide a reasonable reflectional wave for RQDPM imaging. Therefore, in this situation, RBCs imaging essentially undergoes two transmissions of the illumination wave, as mentioned in Part 3.1. Following the reconstruction procedure of RQDPM, we obtain the phase derivatives of RBCs along the x- and y-axes, as shown in Figure 7A and 7B, in which the directional bright and shadow edges indicate the positive and negative phase derivatives of the RBCs along the shear directions. After integrating the phase derivatives along two orthogonal axes through Equation 3, we obtained eventually the phase distribution of RBCs, as shown in Figure 7C. The distributions of the phase derivative and phase along the black and red lines in Figure 7B and 7C are plotted in Figure 7D, where we can intuitively see the correspondence between their peaks. According to the fact that Hb refractive index has a linear relationship with respect to Hb concentration, the Hb mass per unit area (Hb mass density, HMD, projected to a 2D area along the axial direction) for an RBC is therefore linearly related to the measured phase distribution [48]

$$\sigma(\vec{R}) = \frac{\lambda \cdot \varphi(\vec{R})}{2\pi\beta}. \quad (4)$$

Here, β is 0.237 mL/g in our system [49]. Figure 8E shows the HMD distribution of a representative RBC, which provides both physical and chemical information. Clearly, given the area of a single pixel is S_p, the total Hb mass of an RBC can be computed with

$$M = \frac{\lambda \cdot S_p}{2\pi\beta} \cdot \sum_{\vec{R}} \varphi(\vec{R}), \quad (5)$$

indicating a linear correspondence between the total Hb mass and the total phase of an RBC. The total Hb mass estimation for a cluster of 59 RBCs is performed, and the statistical result is shown in Figure 8B. The result shows an average value of 33.7 ± 14.9 pg (mean ± s. d.), which is in accord well with the earlier published results, for example, 28.7 ± 3.7 pg and 27.0 ± 8.0 pg obtained by a UV microscope in [47] and [50], 32.9 ± 1.24 pg by Fizeau-based interferometry in [51], 28.8 ± 5.6 pg by spectroscopic phase microscopy in [52], and 29.9 ± 4.4 pg by digital holography microscopy in [53]. We note that the error of our method (e.g., 14.9 pg in terms of standard deviation) is a little larger than the above-mentioned methods. This may be caused by the health status of the human body or the region selection of RBCs. The total projection area of an RBC is an important morphology parameter, and it was determined by integrating the area whose phase is above the threshold of 0.1 rad in our experiment. For each of those 59 RBCs, the total projection area is calculated, and the statistics are shown in Figure 8A, along with the mean value of 35.5 ± 9.4 μm^2. The averaged projection area for RBCs was also obtained by deep-ultraviolet microscopy as 33.4 ± 4.5 μm^2 [54], which is consistent with our results. Furthermore, by performing the division of the total Hb mass to the total projection area for every RBC, we get the statistics of the mean HMD value, as

Accepted Article

18640648, ja, Downloaded from https://onlinelibrary.wiley.com/doi/10.1002/jbio.202200325 by Nanjing University Of Science, Wiley Online Library on [12/02/2023]. See the Terms and Conditions (https://onlinelibrary.wiley.com/terms-and-conditions) on Wiley Online Library for rules of use; OA articles are governed by the applicable Creative Commons License

shown in Figure 8C, and the average value for the whole RBCs is 0.9 ± 0.1 pg/μm^2. It is worth noting that there is a simple relationship between the total Hb mass (termed as *M*) and the total projection area (termed as *S*) for an RBC, as shown in Figure 8D. The linear fit indicates that they are related by the expression of M=1.48×S-18.8. Above all, we provide a simpler way of estimating the total Hb mass of an RBC by integrating the cell-occupied area. This method can also be easily realized by other imaging approaches, like a brightfield microscope and a fluorescence microscope.

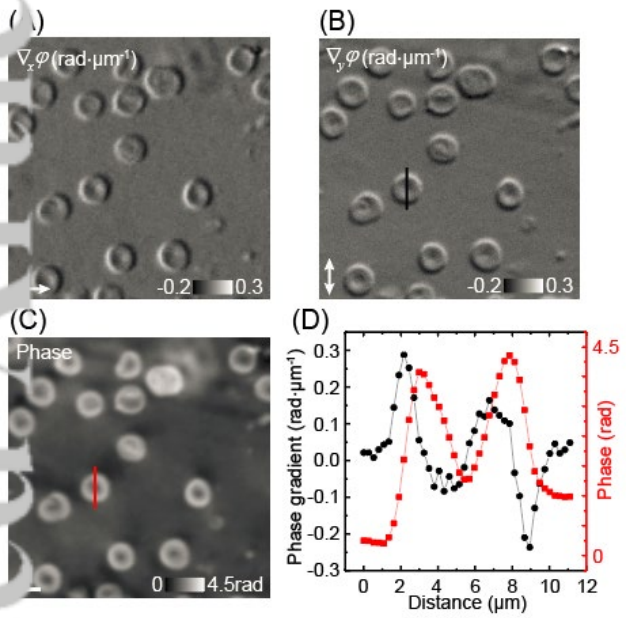

FIGURE 7 Quantitative phase imaging of RBCs by RQDPM. (A) Phase derivative along the *x*-axis. (B) Phase derivative along the *y*-axis. (C) Reconstructed phase map of RBCs. (D) Distributions of phase derivative and phase along the black and red lines in (B) and (C). The scale bar in (C) represents 5 μm.

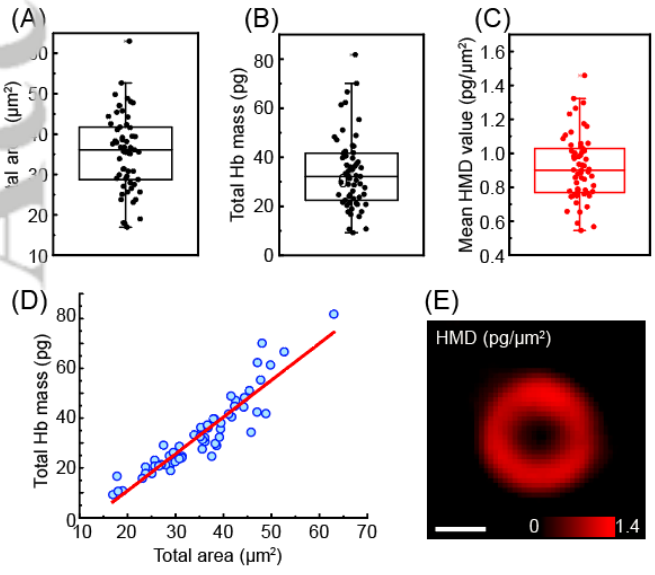

FIGURE 8 Statistics on physical parameters of RBCs. (A) Statistics on total projection area for 59 RBCs. (B) Statistics on total Hb mass for 59 RBCs. (C) Statistics on mean HMD value for 59 RBCs. (D) Linear relation of the total Hb mass to the total projection area of the RBCs. (E) HMD distribution of an RBC. The scale bar in (E) represents 3 μm.

As is well known that quantitative phase imaging has been widely applied in biomedical research, especially in cell tomography, pharmacology, cell biology [10], etc. In the following study, we applied RQDPM equipped with a 20×/0.3 objective lens to quantitative detection of Hela cells that are prepared according to Part 2.3. Similarly, we put the mirror M1 onto the cell-coated glass surface of the petri dish to reflect the object waves. The two images in Figure 9A are the phase derivatives of the transparent Hela cells along the *x*- and *y*-axes, where the insets located in the upper right corner reflect the signal distribution along the two blue lines. The positive and negative changes in the phase derivatives of Hela cells along the two shear directions reflect the effectiveness of RQDPM in visualizing transparent cells. The phase distribution of Hela cells in Figure 9B was then achieved by using Equation 3, where the background has been removed. From the phase image, we can find that there are apparent differences in phase distribution and morphology among different Hela cells in the same petri dish, meaning that cells exist in different states. The most striking phenomenon is that the smaller the cell is, the greater the phase per unit area is.

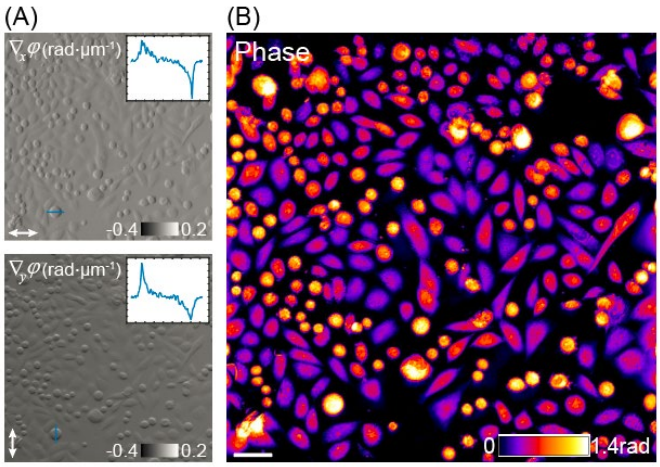

FIGURE 9 Quantitative phase imaging of Hela cells by RQDPM. (A) Phase derivatives along the *x*- and y-axes of Hela cells. (B) Reconstructed phase map of Hela cells with background removed. The scale bar in (B) represents 50 μm.

A quantitative analysis was then performed on a cluster of 266 Hela cells to extract several important parameters. The total projection area of each Hela cell was acquired by selecting the area with the phase value above 0, and the statistical result is shown in Figure 10A. The average total projection area of 266 Hela cells is 368.2 ± 211.9 μm^2 (mean ± s. d.), indicating there is a big variation in total projection

Accepted Article

18640648, ja, Downloaded from https://onlinelibrary.wiley.com/doi/10.1002/jbio.202200325 by Nanjing University Of Science, Wiley Online Library on [12/02/2023]. See the Terms and Conditions (https://onlinelibrary.wiley.com/terms-and-conditions) on Wiley Online Library for rules of use; OA articles are governed by the applicable Creative Commons License

area among the whole cells. Then, the mean phase value per unit area (mean phase density) for each of 266 Hela cells was calculated by dividing the total phase value by the total projection area, and the statistics in Figure 10B tell the mean phase density is 12.5 ± 7.2 rad/μm^2. Moreover, the total projection area and mean phase density were combined for preliminary classification of Hela cells, as is seen in Figure 10C. For convenience, we define a new parameter, circle degree, to further characterize the morphology of Hela cells. The calculation procedure of the circle degree is illustrated in Figure 10D. At first, we identify the coordinates ($\vec{p}_i$, i=1,2,3…) of all the pixels at the edge of the Hela cell by the Sobel operation, and the centroid position ($\vec{O}$) of the Hela cell by the equation of $\vec{O}=\sum(\varphi(\vec{R})\cdot\vec{R})/\sum(\varphi(\vec{R}))$, with $\vec{R}$ being limited to the interior of the cell. Then the distance from an edge pixel of the cell to its centroid is calculated as $d_i=|\vec{p}_i-\vec{O}|$. Finally, the circle degree of the cell is defined as the root mean square error (RMSE) of d_i (i=1,2,3…), which means that the rounder the cell is, the smaller the circle degree is. Figure 10E gives the statistics of circle degree among 266 Hela cells, and the mean value is 1.1 ± 0.9 μm. From the estimation of these parameters, we are assured that our system has great potential in the extraction of parameters of transparent cells, and we believe they will be of importance for biomedical research.

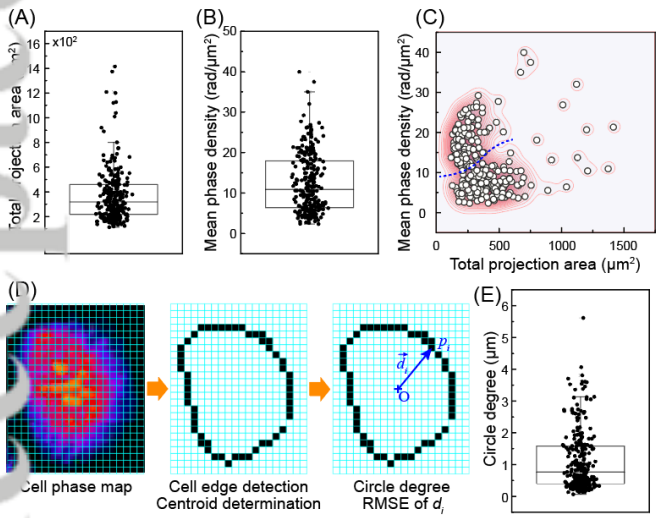

FIGURE 10 Quantitative parameter estimation of Hela cells by RQDPM. Statistical result of total projection area (A) and mean phase density (B) of 266 Hela cells. (C) Preliminary classification of Hela cell based on the total projection area and mean phase density. (D) Calculation procedure of circle degree of a cell. (E) Statistical result of circle degree of 266 Hela cells.

3.5 | Real-time and high-sensitivity flow speed monitoring by using RQDPM in its transmission mode

Microfluidic technique is considered to have great development potential and broad application prospects in biomedical research [55-57]. And highly sensitive quantitative detection of parameters is of extraordinary significance. Since most substances in the microfluidic channels are transparent or translucent, it is hard to capture their flow with traditional methods based on intensity imaging. As mentioned before, our RQDPM can be easily converted into transmission quantitative differential phase microscopy (termed TQDPM) [41]. To be specific, TQDPM shares the identical detection path with RQDPM. TQDPM uses 38 LEDs distributed in a ring as the illuminator that is installed 5 cm above the objective lens, and samples are imaged in the transmission mode. In RQDPM imaging, epi-illumination from a single LED is used (the 38 LEDs will be turned off), and samples are imaged in the reflection mode. The data acquisition and processing in TQDPM is identical with RQDPM.

In this part, we demonstrate that the combination of TQDPM with image correlation analysis can realize real-time and high-sensitivity monitoring of the flow speed of transparent microspheres. In this experiment, the microfluidic channel was formed between two glass-plates, as shown in Figure 11A. The flow speed of the liquid in the microfluidic channel was controlled by an electrical injection system. The flow speed in the observation region indicated with a black box in Figure 11A was adjusted by manually controlling the splitting ratio between the output port and flow-control port. Then, transparent PMMA microspheres with a diameter of 5 μm were diluted into deionized water at a final concentration of ~ 1% and pumped through the microfluidic channel. And the images in Figure 11B are several representative phase images of PMMA microspheres flowing in the microfluidic channel. Since the switching time of the SLM is 3 ms while the exposure time of the sCMOS is 2 ms, we set the framerate of the phase images as 25 frames per second. At such acquisition speed, we continuously captured the flow of the 5-μm PMMA microspheres in the self-built microfluidic channel. The workflow of the flow speed determination process is shown in Figure 11C. First, the GPU-based image correlation was performed between two phase images at two adjacent time points [58]. Second, the position where the image correlation map is the largest was identified as the flow displacement vector of microspheres between two adjacent time points. Third, the mean flow speed in a short time was calculated. Figure 11D shows the variation of the flow speed of the 5-μm PMMA microspheres along the x- and y-axes with respect to time, respectively. It can be seen from Figure 11D that small variation of the flow speed, down to 0.68 μm/s, can be identified by the proposed method.

Accepted Article

18640648, ja, Downloaded from https://onlinelibrary.wiley.com/doi/10.1002/jbio.202200325 by Nanjing University Of Science, Wiley Online Library on [12/02/2023]. See the Terms and Conditions (https://onlinelibrary.wiley.com/terms-and-conditions) on Wiley Online Library for rules of use; OA articles are governed by the applicable Creative Commons License

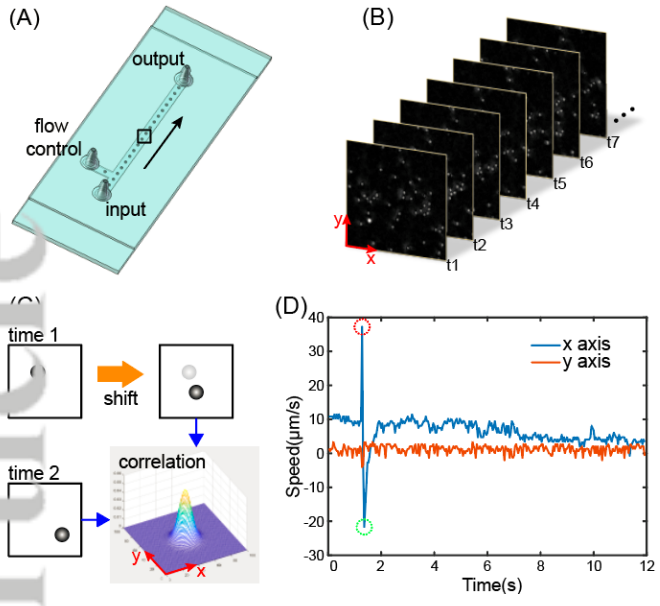

FIGURE 11 Real-time and high-sensitivity flow speed monitoring of transparent PMMA microspheres in a microfluidic channel by combining TQDPM with image correlation operation. (a) Schematic diagram of a self-built microfluidic channel. (b) Representative phase images of 5-μm PMMA microspheres flowing in the microfluidic channel. (c) Schematic of calculating flow displacement vector of the microspheres between two adjacent time points. (d) Variation of the flow speed of the 5-μm PMMA microspheres with respect to time along the *x*- and *y*-axes.

Notably, to test the fast-response ability of the proposed method to detect large-scale speed jumps, we deliberately perturbated the flow control port, and the jumps of the flow-speed were detected, and they were at 1.24 s and 1.32 s, respectively. The two jumps are indicated with the red and green dotted circles in Figure 11D. In addition, the flow process of 5-μm PMMA microspheres accompanied by the real-time and high-sensitivity flow speed monitoring can be found in Visualization 1.

4 | CONCLUSION AND DISCUSSION

In this paper, we introduced a new reflectional quantitative differential phase microscopy (RQDPM) that dexterously exploits the polarization-dependent property of a phase-type SLM. RQDPM is equipped with a partially coherent full-aperture illumination to maximize spatial resolution and suppress multiple scattering of samples. In addition, RQDPM does not require additional special optics, like a Wollaston prism or a grating, to achieve the shear shift between two overlapped object waves, which makes it easier to couple with other imaging modalities. Thus, the compact design of RQDPM makes it easy to integrate into conventional microscopes as a dismountable module.

Owing to the partially coherent full-aperture illumination from a diffused LED, RQDPM has commendable image performance. RQDPM can obtain phase derivatives along any direction by loading different phase masks to the SLM, and it thereby inherits the characteristic of high phase recovery accuracy. Of note, RQDPM has a high axial resolution benefiting from its full-aperture illumination. Thereby, RQDPM provides topography of an opaque semiconductor wafer with a nanoscale axial resolution. Furthermore, RQDPM can be easily switched from reflection mode to transmission mode, and therefore it can be applied to different types of samples. RQDPM facilitates the quantitative imaging of microstructures of thick biological specimens, and several valuable parameters can be obtained to characterize the states of RBCs and Hela cells. For RBCs, we quantitatively showed the HMD distribution and established a linear relationship between the total Hb mass and total projection area for the first time. And for Hela cells, we proposed the new concepts of circle degree and mean phase density for the morphological classification. We hope these parameters can be expanded and used for more kinds of cells for basic life science research and quantified investigation of medical diagnosis. It should be noted that the measured phase value in RQDPM is twice the expected value, which should be divided by 2 to be consistent with its expected value. In addition, RQDPM shares the same detection structure with its transmission mode (TQDPM), and therefore it allows for real-time and high-sensitivity flow speed monitoring of microspheres in a self-built microfluidic channel. This will invite wide applications of TQDPM in online microfluidic detection.

Notably, the partially coherent illumination (PCI) generated by using a rotating diffuser and a laser [18] can simultaneously improve the image quality and the phase modulation accuracy of the SLM in RQDPM. However, the multiple reflections from the optical elements and the sample surface will produce adverse interference patterns. Therefore, it is advantageous to use the partially coherent full-aperture illumination from a diffused narrow-bandwidth LED, which compromises the phase modulation accuracy and the image quality.

Finally, we expect that the proposed RQDPM system with label-free and nondestructive phase imaging features will be a ponderable tool in many kinds of research fields.

ACKNOWLEDGMENTS

This work was supported by the National Natural Science Foundation of China (62105251, 62075177, 12104354); the Natural Science Foundation of Shaanxi Province (2021JQ-184); the National 111 Center; the Fundamental Research Funds for the Central Universities (XJS210503, XJS210504, and QTZX22039), Key Research and Development Program

Accepted Article

18640648, ja, Downloaded from https://onlinelibrary.wiley.com/doi/10.1002/jbio.202200325 by Nanjing University Of Science, Wiley Online Library on [12/02/2023]. See the Terms and Conditions (https://onlinelibrary.wiley.com/terms-and-conditions) on Wiley Online Library for rules of use; OA articles are governed by the applicable Creative Commons License

of China (2022YFE0100700), and Guangdong Basic and Applied Basic Research Foundation (2020A1515110590).

AUTHOR CONTRIBUTIONS

Y. M. performed experiments and data analysis. T. Q. D., L. Y., L. M., S. A., Y. W., J. J. Z., M. L, and C. Z. contributed to data analysis. Y. M. wrote the draft of the manuscript. P. G. and L. K. revised the manuscript.

CONFLICT OF INTEREST

The authors declare no financial or commercial conflict of interest.

DATA AVAILABILITY STATEMENT

The data that support the findings of this study are available from the corresponding author upon reasonable request.

REFERENCES

[1] S. Ranjit, L. Lanzanò, A. E. Libby, E. Gratton, and M. Levi, *Nat. Rev. Nephrol.* **2021**, 17, 128.

[2] N. G. Horton, K. Wang, D. Kobat, C. G. Clark, F. W. Wise, C. B. Schaffer, and C. Xu, *Nat. Photonics* **2013**, 7, 205.

[3] E. Betzig, J. K. Trautman, T. D. Harris, J. S. Weiner, and R. L. Kostelak, *Science* **1991**, 251, 1468.

[4] S. W. Hell and J. Wichmann, *Opt. Lett.* **1994**, 19, 780.

[5] M. J. Rust, M. Bates, and X. W. Zhuang, *Nat. Methods* **2006**, 3, 793.

[6] L. Shao, P. Kner, E. H. Rego, and M. G. Gustafsson, *Nat. Methods* **2011**, 8, 1044.

[7] G. Cennamo, M. Reibaldi, D. Montorio, L. D'Andrea, and M. Triassi, *Am. J. Ophthalmol.* **2021**, 227, 182.

[8] I. Lains, J. C. Wang, Y. Cui, R. Katz, and J. B. Miller, *Prog. Retin. Eye Res.* **2021**, 84, 100951.

[9] T. S. Ralston, D. L. Marks, P. S. Carney, and S. A. Boppart, *Nat. Phys.* **2007**, 3, 129.

[10] Y. K. Park, C. Depeursinge, and G. Popescu, *Nat. Photonics* **2018**, 12, 578.

[11] V. Micó, J. J. Zheng, J. Garcia, Z. Zalevsky, and P. Gao, *Adv. Opt. Photonics* **2019**, 11, 135.

[12] J. Verduijn, L. Van der Meeren, D. V. Krysko, and A. G. Skirtach, *Cell Death Discov.* **2021**, 7, 1.

[13] P. Gao and C. Yuan, *Light: Advanced Manufacturing* **2021**, 3, 105.

[14] M. L. Zhang, Y. Ma, Y. Wang, K. Wen, J. J. Zheng, L. X. Liu, and P. Gao, *Opt. Express* **2020**, 28, 29775.

[15] G. Popescu, T. Ikeda, R. R. Dasari, and M. S. Feld, *Opt. Lett.* **2006**, 31, 775.

[16] Y. Cotte, F. Toy, P. Jourdain, N. Pavillon, D. Boss, P. Magistretti, P. Marquet, and C. Depeursinge, *Nat. Photonics* **2013**, 7, 113.

[17] D. Dong, X. Huang, L. Li, H. Mao, Y. Mo, G. Zhang, Z. Zhang, J. Shen, W. Liu, Z. Wu, G. Liu, Y. Liu, H. Yang, Q. Gong, K. Shi, and L. Chen, *Light-Sci. Appl.* **2020**, 9, 1.

[18] K. Zhuo, Y. Wang, Y. Wang, K. Wen, M. Liu, Y. Ma, J. J. Zheng, and P. Gao, *Front. Phys-Lausanne* **2021**, 9, 796935.

[19] M. Schnell, S. Gupta, T. P. Wrobel, M. G. Drage, R. Bhargava, and P. S. Carney, *Optica* **2020**, 7, 1173.

[20] A. Pan, C. Zuo, and B. L. Yao, *Rep. Prog. Phys.* **2020**, 83, 096101.

[21] G. A. Zheng, R. Horstmeyer, and C. Yang, *Nat. Photonics* **2013**, 7, 739.

[22] S. Song, J. Kim, S. Hur, J. Song, and C. Joo, *ACS Photonics* **2021**, 8, 158.

[23] P. C. Konda, L. Loetgering, K. C. Zhou, S. Q. Xu, A. R. Harvey, and R. Horstmeyer, *Opt. Express* **2020**, 28, 9603.

[24] H. Lee, B. H. Chon, and H. K. Ahn, *Opt. Laser. Eng.* **2021**, 138, 106418.

[25] H. Lee, B. H. Chon, and H. K. Ahn, *Opt. Express* **2019**, 27, 34382.

[26] M. Chen, Z. F. Phillips, and L. Waller, *Opt. Express* **2018**, 26, 32888.

[27] L. Tian and L. Waller, *Opt. Express* **2015**, 23, 11394.

[28] W. Song, A. Matlock, S. Fu, X. D. Qin, H. Feng, C.V. Gabel, L. Tian, and J. Yi, *Opt. Lett.* **2020**, 45, 1647.

[29] C. Zuo, J. J. Li, J. S. Sun, Y. Fan, J. L. Zhang, L. P. Lu, R. N. Zhang, B. W. Wang, L. Huang, and Q. Chen, *Opt. Laser. Eng.* **2020**, 135, 106187.

[30] Y. Li, J. L. Di, C. J. Ma, J. W. Zhang, J. Z. Zhong, K. Q. Wang, T. L. Xi, and J. L. Zhao, *Opt. Express* **2018**, 26, 586.

[31] A. Descloux, K. Grußmayer, E. Bostan, T. Lukes, A. Bouwens, A. Sharipov, S. Geissbuehler, A.-L. Mahul-Mellier, H. A. Lashuel, M. Leutenegger, and T. Lasser, *Nat. Photonics* **2018**, 12, 165.

[32] J. K. Zhang, Y. R. He, N. Sobh, and G. Popescu, *APL Photonics* **2020**, 5, 5040805.

[33] X. Chen, M. E. Kandel, and G. Popescu, *Adv. Opt. Photonics* **2021**, 13, 353.

[34] Y. Ma, S. Y. Guo, Y. Pan, R. Fan, Z. J. Smith, S. Lane, and K. Q. Chu, *J. Biophotonics* **2019**, 12, e201900011.

[35] S. Y. Guo, Y. Ma, Y. Pan, Z. J. Smith, and K. Q. Chu, *Biomed. Opt. Express* **2021**, 12, 4363.

[36] Y. Ma, T. Dai, Y. Lei, J. J. Zheng, M. Liu, B. Sui, Z. J. Smith, K. Q. Chu, L. Kong, and P. Gao, *Opt. Express* **2022**, 30, 9505.

[37] Y. Ma, Y. Wang, L. Ma, J. J. Zheng, M. Liu, and P. Gao, *Appl. Opt.* **2022**, 61, 3641.

Accepted Article

18640648, ja, Downloaded from https://onlinelibrary.wiley.com/doi/10.1002/jbio.202200325 by Nanjing University Of Science, Wiley Online Library on [12/02/2023]. See the Terms and Conditions (https://onlinelibrary.wiley.com/terms-and-conditions) on Wiley Online Library for rules of use; OA articles are governed by the applicable Creative Commons License

[38] T. H. Nguyen, M. E. Kandel, M. Rubessa, M. B. Wheeler, and G. Popescu, *Nat. Commun.* **2017**, 8, 1.

[39] M. E. Kandel, C. Hu, G. N. Kouzehgarani, E. Min, K. M. Sullivan, H. Kong, J. M. Li, D. N. Robson, M. U. Gillette, C. Best-Popescu, and G. Popescu, *Nat. Commun.* **2019**, 10, 1.

[40] P. Bon, G. Maucort, B. Wattellier, and S. Monneret, *Opt. Express* **2009**, 17, 13080.

[41] Y. Ma, L. Ma, M. Liu, J. J. Zheng, S. An, J. Li, and P. Gao, *Opt. Commun.* **2022**, 522, 128685.

[42] R. T. Frankot and R. Chellappa, *IEEE Trans. Pattern Anal. Mach. Intell.* **1988**, 10, 439.

[43] Y. Ma, L. Ma, J. Zheng, M. Liu, Z. Zalevsky, and P. Gao, *Front. Phys-Lausanne* **2022**, 10, 892529.

[44] M. Mir, K. Tangella, and G. Popescu, *Biomed. Opt. Express* **2011**, 2, 3259.

[45] D. H. Tycko, M. H. Metz, E. A. Epstein, A. Grinbaum, *Appl. Opt.* **1985**, 24, 1355.

[46] E. Schonbrun, R. Malka, G. D. Caprio, D. Schaak, and J. M. Higgins, *Cytom. Part A* **2014**, 85, 332.

[47] N. Kaza, A. Ojaghi, and F. E. Robles, *J. Biomed. Opt.* **2021**, 26, 086501.

[48] G. Popescu, Y. K. Park, N. Lue, C. Best-Popescu, L. Deflores, R. R. Dasari, M.S. Feld, and K. Badizadegan, *Am. J. Physiol-Cell Ph.* **2008**, 295, C538.

[49] G. Popescu, *Quantitative Phase Imaging of Cells and Tissues*, McGraw-Hill, New York, **2011**.

[50] M. C. Cheung, R. LaCroix, B. K. McKenna, L. Liu, J. Winkelman, and D. J. Ehrlich, *Cytometry A* **2013**, 83A, 540.

[51] H. Z. Liu, X. Y. Wu, G. D. Liu, H. L. Ren, R. V. Vinu, Z. Y. Chen, and J. X. Pu, *J. Biophotonics* **2022**,15, e202100400.

[52] Y. K. Park, T. Yamauchi, W. Choi, R. Dasari, and M. S. Feld, *Opt. Lett.* **2009**, 34, 3668.

[53] B. Rappaz, A. Barbul, Y. Emery, R. Korenstein, C. Depeursinge, P. J. Magistretti, and P. Marquet, *Cytometry A* **2008**, 73A, 895.

[54] A. Ojaghi, G. Carrazana, C. Caruso, A. Abbas, D. R. Myers, W. A. Lam, and F. E. Robles, *Proc. Natl. Acad. Sci. U. S. A.* **2020**, 117, 14779.

[55] Y. Zhao, Q. Li, X. Hu, and Y. Lo, *Biomicrofluidics* **2016**, 10, 064119.

[56] T. Ghonge, H. C. Koydemir, E. Valera, J. Berger, C. Garcia, N. Nawar, J. Tiao, G. L. Damhorst, A. Ganguli, and U. Hassan, *Analyst* **2019**, 144, 3925.

[57] D. Dannhauser, D. Rossi, F. Causa, P. Memmolo, A. Finizio, T. Wriedt, J. Hellmers, Y. Eremin, P. Ferraro, and P. A. Netti, *Lab Chip* **2015**, 15, 3278.

[58] J. Blaber, B. Adair, and A. Antoniou, *Exp. Mech.* **2015**, 55, 1105.

SUPPORTING INFORMATION

Additional Supporting Information may be found online in the supporting information tab for this article.

Accepted Article

18640648, ja, Downloaded from https://onlinelibrary.wiley.com/doi/10.1002/jbio.202200325 by Nanjing University Of Science, Wiley Online Library on [12/02/2023]. See the Terms and Conditions (https://onlinelibrary.wiley.com/terms-and-conditions) on Wiley Online Library for rules of use; OA articles are governed by the applicable Creative Commons License